Estimation of the Eddy Viscosity Profile in the Sea Surface Boundary Layer from Underway ADCP Observations

ALEXEI SENTCHEV,[a] MAX YAREMCHUK,[b] DENIS BOURRAS,[c] IVANE PAIRAUD,[d] AND PHILIPPE FRAUNIÉ[c]

[a] *Laboratory of Oceanology and Geosciences, UMR8187, Univ. Littoral Côte d'Opale, CNRS, Univ. Lille, IRD, Wimereux, France*
[b] *Naval Research Laboratory, Stennis Space Center, Mississippi*
[c] *Mediterranean Institute of Oceanography, Aix-Marseille University, University of Toulon, CNRS, IRD, Marseille, France*
[d] *LOPS, IFREMER, CNRS, UBO, IRD, Plouzané, France*

(Manuscript received 28 July 2022, in final form 31 January 2023, accepted 26 April 2023)

ABSTRACT: A method of assessing the mean eddy viscosity profile (EVP) in the sea surface boundary layer (SBL) under variable wind conditions is proposed. Performance of the method is tested using observations by an ADCP-equipped platform in the coastal environment of the northwestern Mediterranean Sea under variable (3–12 m s^{-1}) wind conditions. EVP retrievals are made by a variational method strongly constrained by the Ekman dynamics, with the wind and velocity observations assumed to be uncertain within the prescribed error bars. Results demonstrate a reasonable agreement of the EVPs with KPP shape functions for stronger (8–12 m s^{-1}) wind conditions and appear to be consistent with the classical Pacanowski–Philander parameterization of the viscosity profile based on the Richardson number. For weaker (3–5 m s^{-1}) winds, the EVP retrievals turn out to be less accurate, which is primarily attributed to the decay of the wind-driven turbulence energy in the SBL. Feasibility and prospects of the retrieval technique are discussed in the context of uncertainties in the structure of the background flow and limitations of the microstructure and ADCP profiling.

KEYWORDS: Turbulence; Mixing; In situ oceanic observations; Oceanic profilers

1. Introduction

Eddy viscosity in the surface boundary layer (SBL) is a key quantity controlling the momentum transfer between the ocean and atmosphere. As a consequence, considerable efforts are made to parameterize eddy viscosity profiles (EVPs) that may be derived from observations, from model output fields, or from a combination of both. The existing parameterizations vary in complexity from simple algebraic expressions (Jones 1973; Pacanowski and Philander 1981; Peters et al. 1988) to more elaborate algorithms involving heuristic nonlocal parameterization schemes (e.g., Large et al. 1994) and evolution equations for the second-order turbulent moments (e.g., Mellor and Yamada 1982). Although most of these schemes were derived from historical data that have low vertical resolution, specifically close to the surface, direct retrievals of EVPs from in situ observations of the oceanic boundary layers are gaining more attention with the advancing observational techniques and improved data processing methods. These new techniques can be helpful to refine the existing schemes.

In particular, reconstruction of the EVP in the bottom boundary layer (BBL) from ADCP observations has been a subject of intense research in recent years (Yoshikawa and Endoh 2015; Cao et al. 2017). The methodology used is based upon the assumption that the background current near the bottom is nearly barotropic (i.e., it weakly depends on the vertical coordinate), and thus the variation of the horizontal velocity within a 30–50-m-thick layer above the bottom can be largely attributed to the turbulent momentum flux in the BBL. As a consequence, removing the velocity value observed 30–50 m above the bottom yields the velocity profile mostly balanced by the BBL vertical momentum diffusion, thus allowing a direct in situ estimate of the respective EVP with reasonable accuracy.

The situation becomes more complicated in the SBL, where the background current contains a considerable baroclinic (depth-varying) component and velocity observations at the surface may have large uncertainties. As a consequence, estimation of the velocity profile attributed to the vertical turbulent momentum flux becomes more problematic in the SBL. Yu and O'Brien (1991) were probably the first who tried to retrieve the mean EVP in the SBL from moored velocity observations by removing the background flow through filtering of the observed currents in time. Similar types of velocity data (from bottom-mounted ADCP profilers) were used for reconstructing the mean eddy viscosity in the SBL by other authors (e.g., Chereskin 1995; Zhang et al. 2009; Zhang et al. 2015). However, to the best of our knowledge, no attempts have been made to retrieve EVPs directly from underway ADCP observations performed with high vertical resolution down from the sea surface.

In the present study, we explore a possibility to recover variations of the mean vertical viscosity profile by parameterizing the momentum flux driven by turbulent motions at scales within the ranges of 1–10 m in the vertical and 0.1–1 km in the horizontal. We use observations obtained by the platform Coastal Ocean Current Observing System (COCOS) operating in both towed and free drifting modes, which has been previously deployed in coastal ocean regions for high-resolution velocity profiling (e.g., Sentchev and Yaremchuk 2016; Sentchev et al. 2017, 2020). The data used in this study were collected on 11–14 September 2017 in the Bay of Hyères, located in the northwestern Mediterranean (Fig. 1) and referred to hereafter

Corresponding author: Alexei Sentchev, alexei.sentchev@univ-littoral.fr

DOI: 10.1175/JTECH-D-22-0083.1

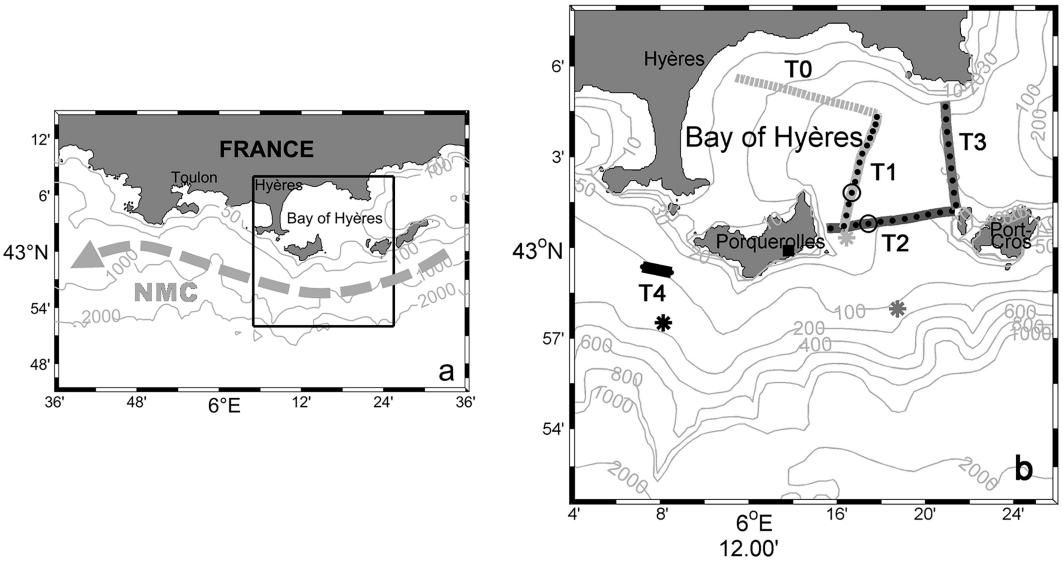

FIG. 1. (a) Location of the study area (black rectangle) in the northwestern Mediterranean and the bathymetry map. Typical location of the North Mediterranean Current (NMC) is shown by gray dashed line. (b) Transects of the towed ADCP platform COCOS on 11, 13, and 14 Sep 2017 are shown by light gray, dark gray, and black lines, respectively, and labeled by T1–T4. Gray dashed line T0 shows the complementary velocity transect on 11 Sep. On 14 Sep, the velocity measurements were performed from the platform freely drifting with currents outside of the bay. Black dots show the locations of 5-min-averaged velocity profiles on the four transects (T1–T4) used in the analysis. Circled dots show the locations of two specific profiles discussed in section 3b. CTD station locations are shown by stars (light gray, dark gray, and black colors matches the three dates of measurements). The meteorological station at the Porquerolles Island is marked by the black square. Bathymetry contours are shown in light gray. Geographic names used in the text are also shown.

as BoH. A strong mistral event occurred during the observation period: the westerly winds increased from 3 to 15 m s^{-1}, causing a complex background flow pattern in and out of the bay, driven by the larger-scale upwelling in the open sea. Viscosity retrievals were made by means of a variational data assimilation scheme strongly constrained by the Ekman dynamics, with the wind and velocity observations assumed to be uncertain within the prescribed error bars.

The paper is organized as follows: In section 2 we provide the general description of the observational platforms, data, and environmental conditions. Section 3 outlines the preprocessing techniques together with the viscosity retrieval algorithm. In section 4 we present the results of vertical viscosity and wind retrievals under different atmospheric forcing conditions and validate our results against the viscosity and wind stress estimates obtained using known parameterization schemes. Conclusions and discussion of further development of the technique are presented in section 5.

2. Data

a. Study site and environmental conditions

The study was conducted on 11–14 September 2017 in the Bay of Hyères located in the northwestern Mediterranean (Fig. 1). The region is characterized by a narrow continental margin, delimited by the 50-m isobath with the depth rapidly increasing from 100 to 2000 m farther offshore. The main feature of the local circulation is the North Mediterranean Current (NMC)—a westward slope current, which is a part of the general circulation of the western Mediterranean (Millot 1999). The NMC dynamics is controlled by complex topography and by winds with the dominant direction either from the west or from the east (Guihou et al. 2013; Marmain et al. 2014). During the study, the NMC was characterized by a 20-km-wide westward flow with a typical surface velocity of 0.2 m s^{-1}. Tidal motions are negligible in the study area.

The Bay of Hyères is a semienclosed and shallow-water area, approximately 20 km × 15 km. A number of islands delimit the bay in the south, with the biggest one, Porquerolles, located in its southwestern part. The local bathymetry gradually increases from 10 m, in the bay head, to 50 m, within the southern and eastern narrows (Fig. 1). Farther offshore, steeper bathymetry of the continental slope marks the location of NMC.

The study was conducted during a mistral event, an upwelling favorable wind, regularly observed east of the Rhone River mouth, where it mainly has a southward direction. The mistral is often violent and dry, reaching up to hundreds of kilometers offshore (Jansá 1987). It is associated with clear skies and may happen in any season, but with more frequent occurrence in winter (Givon et al. 2021). The mistral blows with gusts that can exceed 25 m s^{-1}, with average speeds of 10–15 m s^{-1} during the day, decreasing significantly at night (Millot 1979). In the easternmost part of the Gulf of Lions, affected by local orographic features, the mistral veers eastward, blowing along the shore, and generates coastal upwelling. Being strong, cold, and dry, it enhances air–sea heat fluxes and therefore accelerates the reduction of sea surface temperature (Flamant 2003).

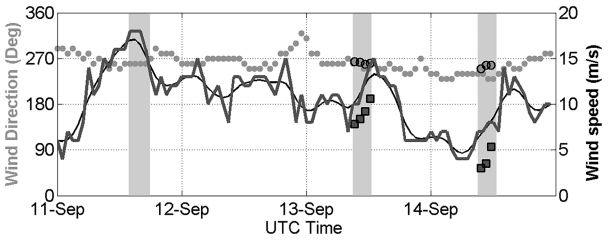

FIG. 2. Hourly mean wind speed (dark gray) and wind direction (light gray dots) at the Porquerolles Island meteorological station and from anemometer observations 2 m above the sea surface (gray squares and circles). Smoothed wind speed is shown by thin black line. Periods of ADCP transect surveys are shown by light gray shading.

b. Observations

1) WIND OBSERVATIONS

The hourly wind data were provided by the meteorological station located 140 m above the sea level at the Porquerolles Island. In addition, on 13 and 14 September, the wind speed was measured 2 m above the sea surface by a sonic anemometer mounted on the free drifting experimental platform OCARINA (Bourras et al. 2019). Figure 2 shows that the wind speed recorded at the island exceeds sea surface observations by approximately 2–4 m s^{-1}. At the same time, the wind speed time series from both sources show similar variability which gives certain confidence in the data. In general, observations demonstrate a sustainable eastward wind during the entire study period. The variation of the wind speed (shown by the gray solid line in Fig. 2) was more pronounced than that of the wind direction. In particular, the strongest wind (15–18 m s^{-1}) was observed at 1100–1700 UTC 11 September, during the first transect survey (T0–T1). Another noticeable event occurred on 13 September, when the wind increased from 7 to 14 m s^{-1} in just a few hours during the second transect survey (T2–T3). In between these two events, the wind speed exhibited large variability within the range of 7–15 m s^{-1} (Fig. 2). The weakest wind (4 m s^{-1}) was detected in the morning of 14 September followed by a gradual rise of the speed in the afternoon during the third survey (T4). The observed changes in the ocean–atmosphere flux of momentum and related changes in the ocean surface boundary layer were assessed by analyzing velocity profiles from transect surveys shown in Fig. 1 and marked by gray shading in Fig. 2.

2) VELOCITY MEASUREMENTS

Underway velocity profiling was performed by the experimental platform COCOS towed by the R/V *Tethys-II*. The platform, featuring two cylindrical hulls 1.80 m long and 0.2 m in diameter, connected by a 0.8 m × 0.8 m stainless steel frame, was carrying a surface mounted broadband ADCP (600 kHz Teledyne WorkHorse Sentinel). The distance from the R/V central axis was controlled by an adjustable side fin making it possible to avoid contamination from the wake of the vessel. The ADCP's transducer head was located 0.3 m below the water surface. The blanking was set to 0.4 m, the bin size to 0.5 m, and the center of the first bin was roughly at 1 m below the water surface. The profiles were acquired down to the depth 35–37 m. The ADCP was set to operate at the pinging rate of 1 Hz. Each ping for velocity was composed of three subpings averaged within 1-s interval, providing a velocity error of 0.04 m s^{-1}. Single-ping bottom tracking was enabled to correct for the boat's movement, and the recorded velocities formed a current vector in the fixed frame relative to the bottom. The vessel's speed was typically 2 m s^{-1} for the majority of transects. The ADCP data were merged with the navigation data provided by onboard GPS system, also operating at 1 Hz.

On 14 September, under calm wind conditions, the velocity profiling was performed from the freely drifting platform, which was attached to OCARINA, performing wind observations at the air–sea interface. The drift lasted slightly more than 3 h yielding an approximately 1.5-km-long velocity transect (T4 in Fig. 1b). Additionally, the OCARINA platform performed a 4-h drift inside the BoH on 13 September, recording atmospheric parameters at the air–sea interface during the towed transects T2 and T3.

3) TEMPERATURE AND SALINITY

Three CTD profiles were acquired by a Sea-Bird SBE19, one profile for each day of the survey (at 1630 UTC 11 September, 1630 UTC 13 September, and 1300 UTC 14 September). Temperature and density profiles clearly show the surface mixed layer with a homogeneous temperature distribution during two surveys performed under strong wind conditions on 11 and 13 September (Fig. 3). The mixed layer appears eroded on 14 September due to significant wind decrease at nighttime. The patterns of density variation with depth generally follow temperature profiles, indicating dominance of the thermal contribution to the stratification. The mixed layer depth h, referred hereafter as MLD, is defined as the top of the thermocline. Furthermore, we assume that MLD derived from the density profiles provides a good assessment of the SBL thickness, which is conventionally estimated by the vertical extent of the quasi-homogeneous density structure (e.g., Belcher et al. 2012).

The time evolution of temperature profiles demonstrates a significant (1°C) decrease in the SBL heat content between 11 and 13 September (Fig. 3) under strong winds, followed by a smaller temperature decrease caused by the mistral relaxation on 14 September (Fig. 2). As a result, the mixed layer thickness decreased by 5 m between 11 and 13 September, and then the layer started to disintegrate but still kept its overall trend of heat content reduction.

Underway measurements of sea surface temperature (SST) were also performed during the surveys by a SeaCat thermosalinograph (Sea-Bird SBE-21) mounted on board of the R/V *Téthys-II*. SST measurements (not shown) further confirmed the surface cooling trend over the entire bay and in the adjacent open sea region to the south.

3. Methodology

During the study period, circulation in the bay was driven by winds with a typical time variability of 10–15 h (Fig. 2). We

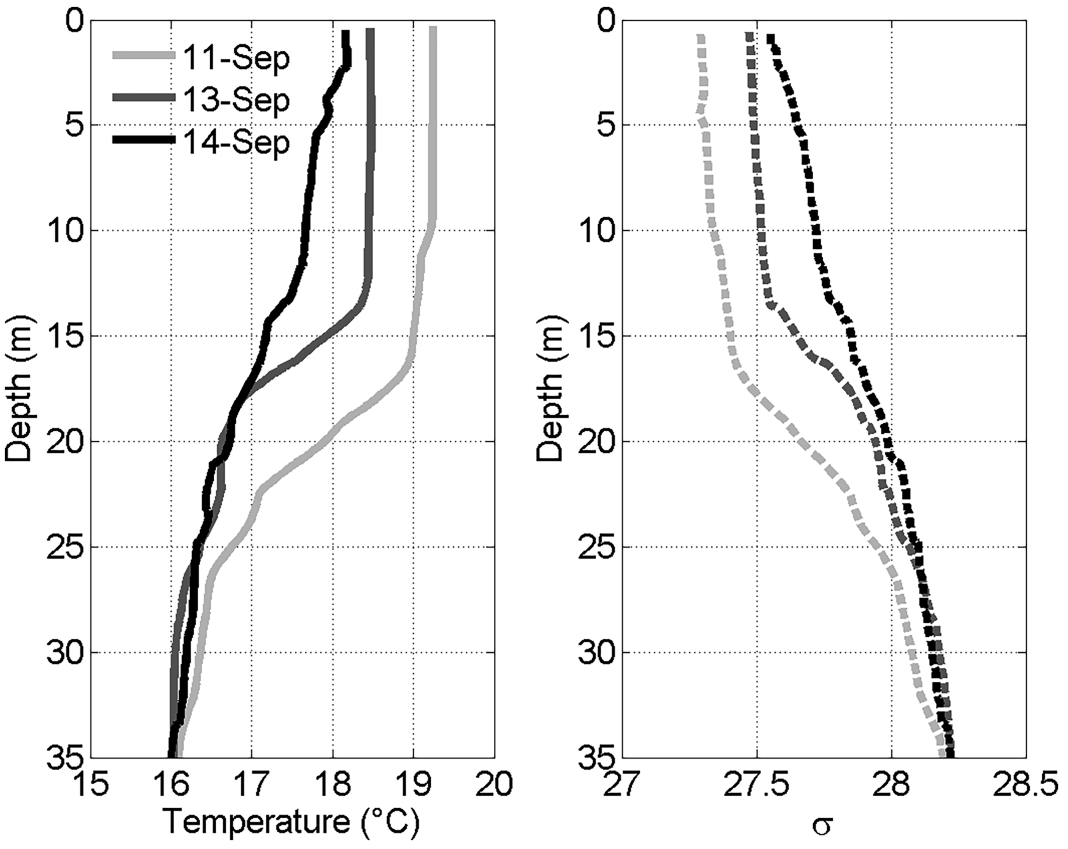

FIG. 3. (left) Temperature and (right) specific density profiles for each surveying day. Profile locations in both space and time are shown using the same colors of the stars in Fig. 1.

focus on the estimation of vertical momentum flux in the ocean surface boundary layer assuming that the wind-induced turbulent mixing adjustment in the Ekman layer occurs at a time scale of $f^{-1} \sim 3$ h and thus it can be captured by the towed ADCP transects, making it possible to employ the Ekman balance constraints as a dynamical filter to retrieve the EVPs. At the same time, velocity patterns from the transect surveys revealed a wind-driven background circulation strongly constrained by the peculiarities of coastal topography and bathymetry. The most prominent feature of this flow is a two-layer circulation with a significant velocity shear, specifically in the top 10 m of the water column (Fig. 4). Performing the analysis, we first attempted to remove the background flow from the observed velocity profiles prior to applying the viscosity retrieval algorithm. This strategy was not successful, mostly due to large space–time variations of the background circulation and to errors in the vertical velocity gradients introduced by the heuristic methods of approximating the background flow. An alternative approach, in which the Ekman currents were retrieved first, and the background current was

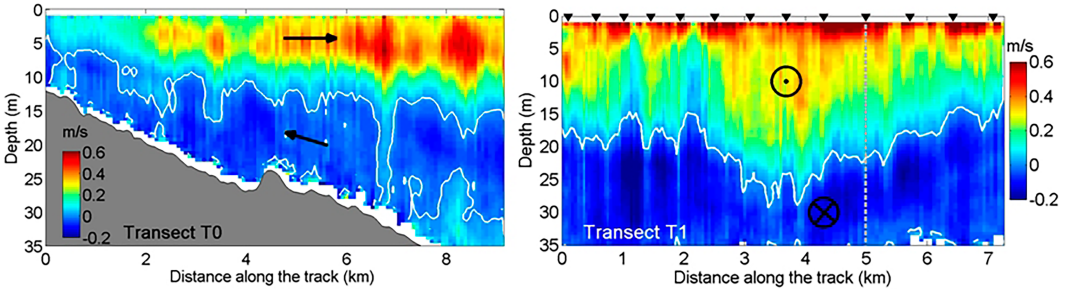

FIG. 4. Current velocity variation (left) along the transect T0 and (right) across the transect T1 on 11 Sep 2017. Arrows and symbols show the mean flow direction. Triangles at the top mark the locations of 5-min-averaged velocity profiles used in the analysis. The vertical gray line in the right panel shows the location of profile 10 on T1. The zero-velocity contour line is given in white. See Fig. 1 for the transect locations.

diagnosed in the second step, was found to be more efficient, because the EVPs and the optimized wind stress obtained after the first step were not affected by the choice of the background flow approximation.

a. Velocity preprocessing

The velocity data from three ADCP transects (T1–T3) were used to estimate the depth variation of the vertical viscosity coefficient $\nu(z)$ and the wind stress. Additionally, we used the data from the fourth transect (T4) which took place outside of the bay on 14 September, under relatively weak (3–5 m s^{-1}) westerly winds. These four transects were selected for SBL viscosity retrievals because the transect surveys were done in water deeper than 40 m, and therefore, the velocity profiles were less affected by the influence of the bottom boundary layer.

The individual profiles, sampled at 1-s resolution, were time averaged within 5-min intervals on the transects T1–T3, when the ADCP platform was towed. Velocity profiles obtained by the freely drifting platform on 14 September, were additionally averaged within the 20-min time intervals, which roughly corresponds to the integral time of turbulence in the lower atmosphere (e.g., Bourras et al. 2019). This provided us with the horizontal velocity profiles $\mathbf{u}_{\mathrm{obs}}(z)$ in 10–13 nearly regularly spaced locations on the transects T1–T3 at approximately 500-m horizontal resolution, and at 150-m resolution on the transect T4 (Fig. 1b). In the vertical, the averaged velocity data were kept in the original bins with 0.5-m spacing. The analyzed profiles had 70 points in the vertical stretching down from 1 to 35 m below the surface.

b. Assessing the background flow and velocity shear

The ADCP transects revealed a distinct two-layer circulation in the BoH. Under persistently strong westerly wind, the flow direction in the surface layer is globally southward and the Ekman transport discharges water out of the bay through the southern narrow. This generates a return flow in the subsurface layer, directed from the open sea into the bay, and an upward motion, which are well captured by the transect survey on 11 September. Such two-layer circulation is a characteristic feature of coastal upwelling (Cushman-Roisin et al. 1994). Figure 4 provides an example of the velocity variation along the transects T0 and T1. The circulation pattern (especially T1) demonstrates a strong (up to 0.6 m s^{-1}) outflow from the bay with higher velocity shear in the upper 5–10 m. The deep return current appears to be weaker and somewhat more extended in the vertical with the inflection point at roughly 20 m. The temperature profile recorded at the southern outlet of the bay (cf. Fig. 3) clearly shows that the depth of the current reversal is related to the thermocline location within the water column. Velocity profiles in the shallow part of the bay (transect T0) show more irregular velocity variation with depth, with largest velocities observed at 5 m, and likely divergent surface flow. In the deeper part of the bay (transect T1), most of the spatial variation of velocity is observed in the surface layer (Fig. 4 right panel). In the eastern narrow (transect T3, not shown), the eastward outflow was much shallower, occupying only 5–7 m of the surface layer, and the inflow was observed in the rest of the water column.

The complexity of the background circulation, featuring strong currents, often opposing the wind direction (and the respective Ekman flow), is also visible on the individual (i.e., 5-min-averaged) velocity profiles. As an example, Figs. 5a and 5c show the individual profile at the tenth point on T1 (its location is given in Fig. 1b and also in Fig. 4, right panel) and the transect-averaged velocity profile. Both profiles have similar shape, demonstrating a clear signature of the Ekman current in the surface layer extending down to 25 m. The southward background flow, with large (~0.4–0.6 m s^{-1}) velocities dominates at the intermediate depth (5–15 m). The velocity vector, with maximum velocity (~0.6 m s^{-1}) observed at the surface, veers clockwise with respect to the wind direction, in general agreement with the Ekman theory. At the sea surface, the angle between the flow direction and the wind is close to 30°.

Similarly, the transect-averaged velocity profile and individual profile at point 4 in the southern narrow (transect T2, Figs. 5b,d) both show a combination of the Ekman current and an intense outflow in the surface layer. Due to predominant southward outflow at the bay exit, a larger angle (~50°) is observed between the surface current and the wind direction.

The vertical gradient s of horizontal speed was estimated from the profiles shown in Figs. 5a and 5b using the relationship $s = \sqrt{(\partial u/\partial z)^2 + (\partial v/\partial z)^2}$. The value of s is found to be close to 0.15 s^{-1} in the surface layer 5 m thick, while it is 5 times smaller (0.03 s^{-1}) in the subsurface layer extending down to 25 m, indicating exponential decay of the developed Ekman circulation.

The above preliminary analysis of the ADCP transects demonstrates both significant space–time variations of the background flow and clear signatures of the Ekman currents in the upper layer characterized by a stronger velocity shear. We therefore adopted a strategy to first retrieve Ekman currents from the 5-min-averaged velocity profiles by the adjustment of the vertically varying viscosity coefficient and wind stress and then average the results for each transect to obtain more robust estimates of the viscosity. The approach assumes that dynamical constraints of the variational retrieval algorithm (see appendix) are efficient enough to separate the Ekman-related velocity shear near the surface from the background velocity gradients of the same (or in some locations, even larger) magnitude in the deeper layers.

c. Validation

To validate EVP and wind stress retrievals, we compared the results with existing parameterizations of viscosity and stress that depend on other (directly measured) quantities. In particular, wind observations at the Porqueroles meteorological station were used for independent estimates of the wind speed 10 m above the sea surface (U_{10}), and the wind stress $\boldsymbol{\tau}$. For the wind stress, the bulk formulation (e.g., Smith 1988) was used. The required drag coefficient C_d was assumed to be a quadratic function of U_{10}, based on a recent analysis of an extended dataset of in situ measurements (Bourras et al. 2019):

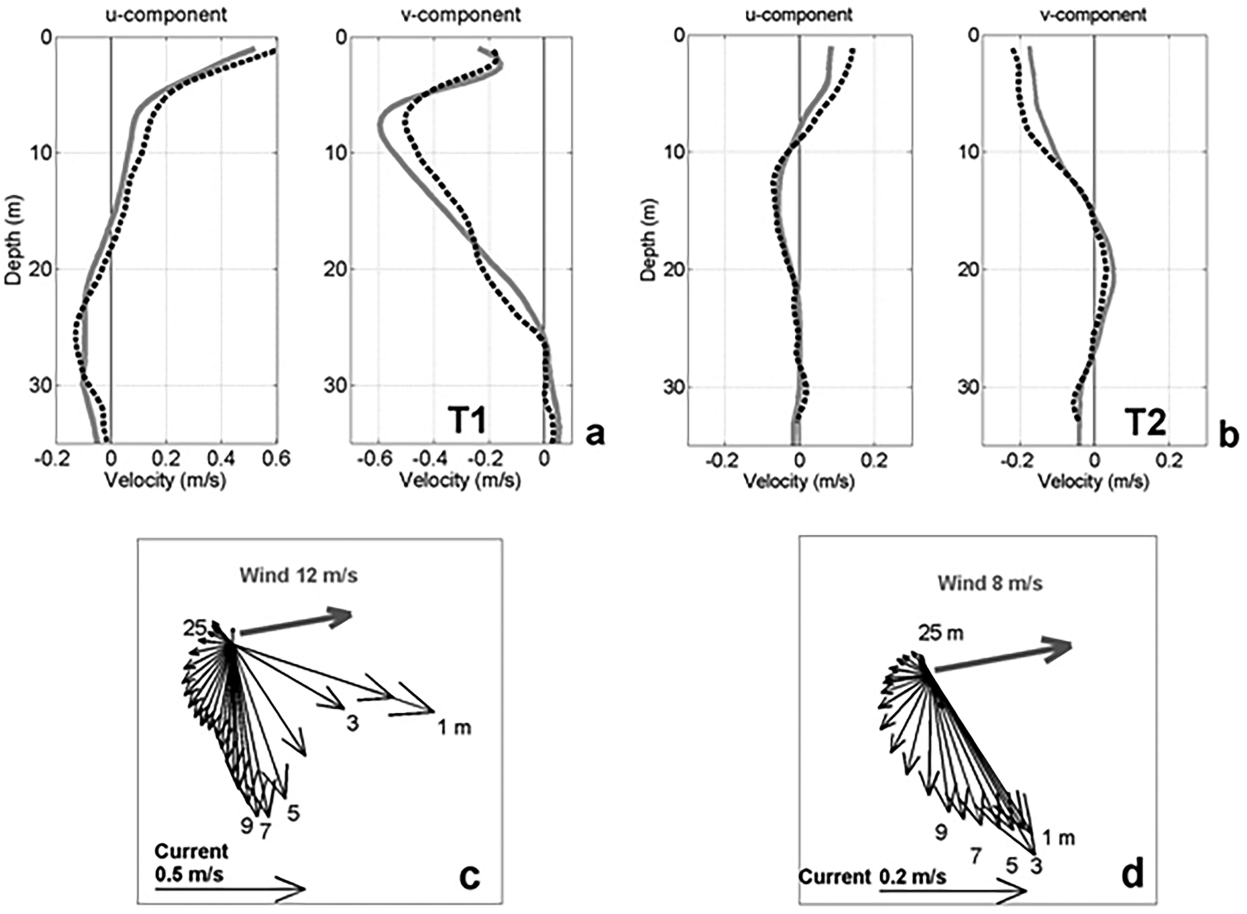

FIG. 5. (top) Transect-averaged velocity profiles for the along- and across-section velocity components (dashed black) on transects (a) T1 and (b) T2, and individual (5-min-averaged) profiles (gray) on T1 (at point 10) and on T2 (at point 4). (bottom) Individual velocity vector profiles (c) at point 10 on T1 and (d) at point 4 on T2. Point 10 and 4 locations are shown in Fig. 1. Numbers in (c) and (d) show depth (in m) of the velocity vectors. Wind direction and wind speed (U_{10}) during the transect surveys are also shown.

$$C_d = 10^{-3}[1.27 + (0.006\,U_{10} - 0.062)U_{10}]. \quad (1)$$

The wind speed U_{10} and wind-induced Ekman current velocity $\mathbf{u}_e$ were also validated against the empirical relationship of Weber (1983) derived on the basis of Lagrangian treatment of the wind-driven motions at the sea surface:

$$|\mathbf{u}_e| \approx 27\sqrt{C_d \frac{\rho_a}{\rho_0}}|U_{10}|, \quad (2)$$

where ρ_a and ρ_0 are the mean air and water densities and U_{10} is estimated from wind observations both at Porqueroles meteorological station and OCARINA platform using a logarithmic wind profile approximation.

As shown in Fig. 3, the upper layer in the BoH, appears to be well mixed down to ~15-m depth. Below this level the enhanced stratification increases the water column stability, which is conventionally quantified by the squared Brunt–Väisälä frequency:

$$N^2 = -(g/\rho_0)\partial\rho/\partial z. \quad (3)$$

On the contrary, the kinetic energy associated with the velocity shear s enforces turbulence production, so that the gradient Richardson number

$$\mathrm{Ri} = N^2/s^2 \quad (4)$$

provides a measure of the relative contributions of buoyancy and velocity shear to the stability of the water column in the surface layer. Since the value of Ri is widely used in numerous viscosity parameterization schemes, we elected to estimate the vertical profiles of Ri for validation of the EVP retrievals. The respective Richardson number profiles were obtained by applying (3) and (4) to the velocity profiles and CTD stations data obtained on the same day, and then the results were averaged over 5-min intervals.

d. Viscosity and wind stress retrievals

To estimate the vertical momentum diffusion coefficient $\nu(z)$ in SBL, we employed the variational optimization algorithm (e.g., Yu and O'Brien 1991) based on the minimization of a quadratic cost function subject to the dynamical constraints

imposed on the velocity profiles by the Ekman dynamics (see appendix for details). The minimization was performed by varying the free parameters, namely, the 60 gridded values of the vertical viscosity coefficient in the upper 30 m and two components of the wind stress. The optimized EVPs and wind stress estimates were retrieved from the corresponding velocity profiles averaged along the transects at 5-min (~150–500-m) resolution. After that, the optimized values of the free parameters were additionally averaged for each transect to obtain more robust values. The error bars for the transect-averaged EVP profiles were computed as 90% confidence limits for the χ^2 distributions with the number of degrees of freedom equal to the number of individual EVP profiles (10–13) averaged along the transect.

The EVP retrieval constitutes the first step of the assessment of circulation in BoH. In the second step, after removing the transect-mean Ekman velocities $\mathbf{u}_e(z)$ from the observed velocity profiles averaged along the transects, the background velocities $\mathbf{u}_b(z)$ were approximated by the third-order polynomial in z. This function is the minimal degree polynomial capable of accounting for the two extrema in the velocity profile corresponding to the two-layer structure of the background circulation. Additionally, the function yields a minimum curvature of the polynomial which is more suitable for approximating the observed profiles.

Finally, for each observed individual velocity profile, the overall relative approximation error was estimated according to

$$\mathrm{err} = \sqrt{\frac{\langle (u_e + u_b - u_{\mathrm{obs}})^2 \rangle}{\langle u_{\mathrm{obs}}^2 \rangle}}. \tag{5}$$

Here the angle brackets denote averaging in the vertical and over the ensemble of profiles for each of the four transects. The error accounts for contributions from other components of the SBL dynamics (e.g., Stokes drift, Langmuir circulation) and for the limitations of the heuristic background current approximation.

To further verify the consistency of the Ekman constraints imposed in our EVP estimation, a comparison was done with two other EVP parameterization schemes. The eddy viscosity coefficient resulting from the current velocity shear has been traditionally related to the Richardson number through an equation of the form (e.g., Pacanowski and Philander 1981)

$$\nu(z) = \nu_b + \nu_0/[1 + \alpha \mathrm{Ri}\ (z)]^n, \tag{6}$$

where ν_0, α, and n are the adjustable parameters; ν_b is a background value of viscosity. The background viscosity ν_b is a rather uncertain parameter with typical values of 0.1–1 cm^2 s^{-1}, which accounts for the background mixing processes occurring even in the absence of any forcing at the surface (e.g., internal wave breaking or larger-scale velocity shear at depth).

In addition, the optimized EVP profiles were compared with those calculated from the K-profile parameterization (KPP) scheme of Large et al. (1994) which includes an empirical algorithm for determining the SBL depth h, where the turbulent contribution to the vertical shear of a bulk Richardson number is parameterized. In this study, the KPP mixed layer depth h was estimated directly from the observed density profiles available for each surveying day. This approach does not require additional calculation of h via (rather uncertain) bulk Richardson number parameterization. Given h, the EVP profile was computed as the product of a depth-dependent turbulent velocity scale w_x and a nondimensional vertical shape function G, both provided in Large et al. (1994). Similar to the independent EVP estimates [Eq. (5)], based on the gradient Richardson number, the KPP-based estimates were averaged for each transect and compared with EVPs retrieved by the variational method.

Finally, we checked robustness of the EVP retrievals, by assessing sensitivity of the method to the errors of velocity observations and the initial choice of the control variables. Results of these experiments (see appendix) demonstrated a reasonably good agreement between the EVPs retrieved from the perturbed observations/parameters and the profiles shown in Fig. 6a.

4. Results

a. Viscosity profiles

Four reconstructed EVPs, averaged for each transect performed under various wind forcing, are shown in Fig. 6. The shape of EVPs is consistent with the basic assumption of viscosity variation with depth: the largest values are found in the mixed layer (ML) with smaller values at the sea surface and below the thermocline. EV decreases with depth in the thermocline (16–25 m, Fig. 6d) where the background flow changes direction and maintains the velocity shear (Fig. 5), but stronger stratification tends to dump turbulence production. Within the mixed layer, EVP tends to have a maximum close to the ML middepth (~0.6 h).

The vertical extent of the layer with large viscosity values varies in time and closely follows the ML evolution in response to wind forcing: the ML extends to 17 m on 11 September (transect T1), and gradually decreases to 13 m on 13 September (transects T2 and T3, respectively). On 14 September, the viscosity profile does not have any distinctive features (Fig. 6e) and appears to have statistically insignificant values throughout the water column. This can be attributed to the rapid decline of the turbulence production under weak atmospheric forcing and gradual restoration of the stratification in SBL (Fig. 6f).

The mean, the standard deviation, and the maximum values of EVPs retrieved from velocity measurements are summarized in Table 1. The maximum EV values in the mixed layer demonstrate profound wind dependence, varying in a wide range from 16 to 18 cm^2 s^{-1}, for the 8–10 m s^{-1} winds, to nearly 40 cm^2 s^{-1}, for the wind speed U_{10} of 12 m s^{-1}. Under milder winds, all quantities characterizing the turbulent mixing are smaller: the maximum EV value drops below 20 cm^2 s^{-1}, while its vertical mean is ~11–13 cm^2 s^{-1} for both transects on 13 September. There is a large difference (by a factor of 2) in EV values under the strong persistent wind observed for several hours on 11 September (Fig. 2) as compared to EVPs retrieved under 30% milder wind conditions on 13 September. Note the

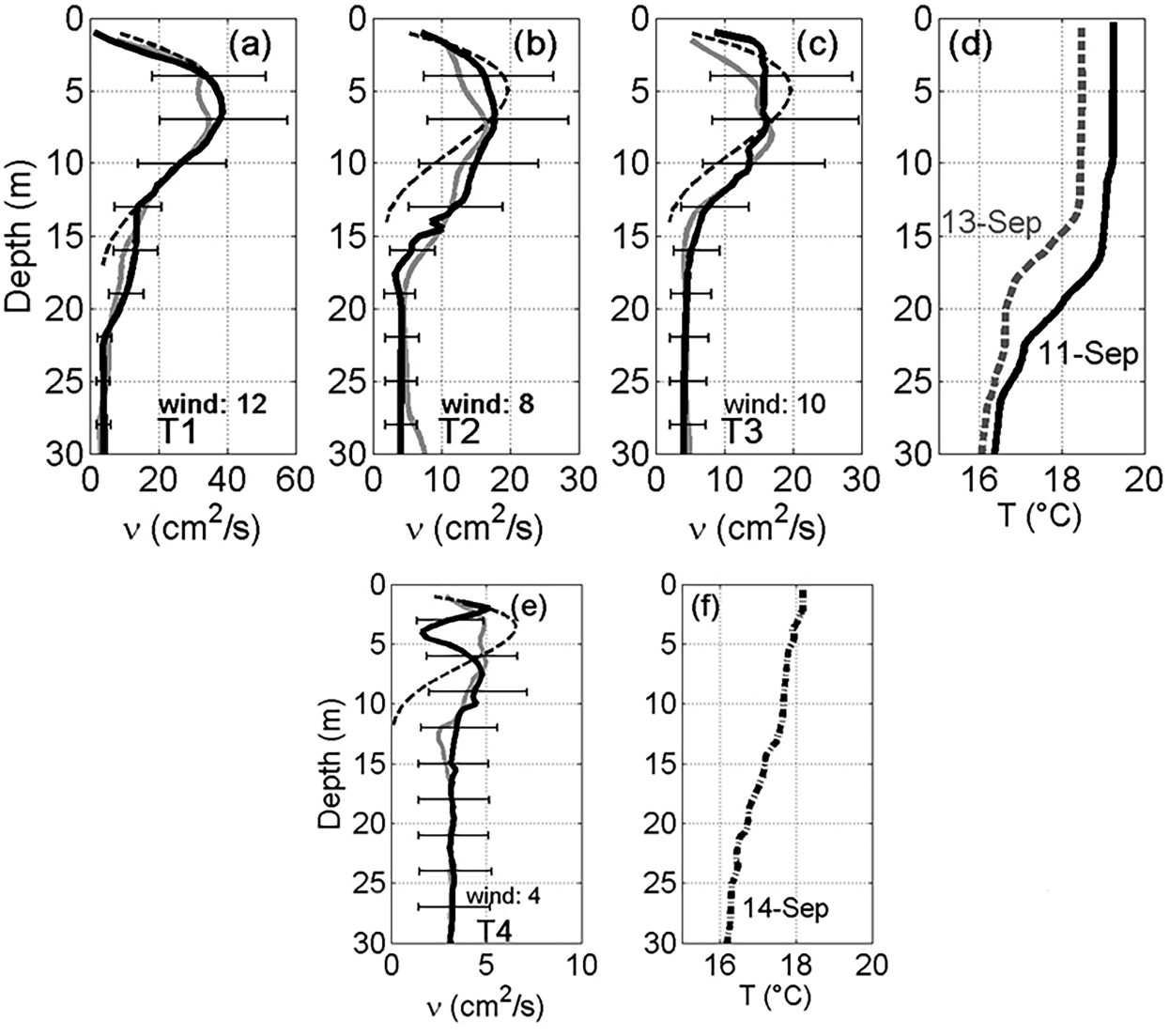

FIG. 6. EVP retrievals for (a) strong, (b),(c) moderate, and (e) weak wind conditions are shown in black. Solid gray lines show the EVPs obtained using Eq. (6), and the dashed lines show EVPs based on the KPP parameterization. (d),(f) Temperature profiles for the three dates of the ADCP surveys are shown for comparison. Wind speeds (U_{10}; in m s^{-1}) at the time of the transect surveys is also shown. Note the difference in horizontal scales for ν between (a), (b), and (e). Horizontal bars show the 90% confidence intervals.

higher accuracy of the EVP retrieval for stronger winds: for surveying days characterized by strong and moderate wind conditions, the depth variation of EV is statistically consistent. In contrast, for milder winds (3–5 m s^{-1}) observed on 14 September, the values of ν and the error bars are on the same order of magnitude. The EV confidence intervals are partly contributed by spatial variability of the EVP along the transects. This variability, compared to the mean, appears

TABLE 1. Optimized viscosities averaged over the observed mixed layer depths h and their approximation errors e by the gradient Richardson and KPP parameterization schemes. The approximation errors were computed as rms deviations of the respective profiles in Fig. 6. The observed values of U_{10} and h are given in the last two columns. Boldface numbers in the first column give the number of profiles used in the EVP retrieval, the date and time of the transect.

Transect	$\langle\nu\rangle_h$ (cm^2 s^{-1})	ν_{max} (cm^2 s^{-1})	e(Ri)	e(KPP)	U_{10} (m s^{-1})	h (m)
T1(**13**), 1400–1500 UTC 11 Sep	24 ± 2.8	39	0.13	0.14	11.6	17
T2(**11**), 1000–1100 UTC 13 Sep	13.4 ± 3.9	18	0.17	0.23	8.2	13
T3(**9**), 1100–1200 UTC 13 Sep	11.4 ± 2.1	16	0.18	0.25	10.1	13
T4(**10**), 0900–1200 UTC 14 Sep	3.7 ± 3.2	5	0.28	0.67	4.3	12

TABLE 2. Estimates of the wind stress τ and the surface Ekman current speed $|\mathbf{u}_e|$ for four transect surveys. Angle shows the difference between the wind and surface current direction. Err is the overall relative error of optimization.

Transect, date	τ^{opt} (N m^{-2})	τ^* (N m^{-2})	τ_O^* (N m^{-2}; OCARINA)	$\|\mathbf{u}_e\|^{opt}$ (cm s^{-1})	$\|\mathbf{u}_e\|^*$ (cm s^{-1})	Angle	Err
T1, 11 Sep	0.12 ± 0.11	0.22	—	35.8 ± 11.1	39	47°	0.55
T2, 13 Sep	0.06 ± 0.05	0.10	0.16	16.2 ± 2.8	26	48°	0.75
T3, 13 Sep	0.08 ± 0.06	0.16	0.22	10.6 ± 3.6	33	65°	0.56
T4, 14 Sep	0.02 ± 0.04	0.03	0.03	4.9 ± 5.9	4	100°–180°	0.83

to be larger along the transect T2 (~13 ± 4, Table 1, line 3) indicating a potential modification of the flow field by local topography in the southern narrow.

Independent EVP estimates obtained by parameterization (6) are shown in gray in Fig. 6 for comparison. The discrepancy between the two methods of EV estimation is quantified and reported in the third column of Table 1. In general, the depth variation of ν(Ri) is in a reasonably good agreement with EVPs retrieved from velocity profiles for stronger (12 m s^{-1}) and moderate (8–10 m s^{-1}) wind conditions (Figs. 6a–c). The obtained values of the parameterization coefficients (ν_o = 50 cm^2 s^{-1}, α = 5, n = 2, ν_b = 2 cm^2 s^{-1}) for stronger winds (transect T1) are in general agreement with those suggested by Pacanowski and Philander (1981) and Yu and Schopf (1997) with the relative error level e(Ri) of only 13% (Table 1, column 3). The value n = 2 of the power coefficient was found to be optimal for all Ri-based EVP parameterizations. For moderate winds observed on 13 September (transects T2 and T3), the best fit of EVP was found for the values ν_o = 50 cm^2 s^{-1}, α = 3.5, and ν_b = 4 cm^2 s^{-1}, with the relative error of 17%. The results of comparison with the parameterization (6) are much worse for the weak unsteady wind on 14 September.

Comparisons of the variational EVP retrievals with those obtained by the KPP scheme of Large et al. (1994) demonstrate a good agreement for the strong wind case (Fig. 6a). The shape of both profiles is nearly identical in the surface mixed layer. A somewhat larger discrepancy is found for weaker winds observed on 13 September (Fig. 6b). In both cases, the depth of maximum turbulent mixing is located around 6 m, as indicated by both profiles. For milder wind (Fig. 6c, transect T3), the location of EVP maximum is captured with less confidence, due to nearly opposite direction of the background flow with respect to the wind at that time. The overall discrepancy between the EVPs for the strong wind (relative error 0.13 reported in Table 1, line 2, column 4) appears to be similar to the Ri-based parameterization of Pacanowski and Philander (1981). For the moderate wind conditions (transects T2–T3) the error increases up to 0.25 (Table 1, line 4, column 4). The ML depth appears slightly shallower (13 m) in response to milder wind. But larger differences in ν (up to 5–7 cm^2 s^{-1}) are observed below this depth on T2 and, to a minor extent, on T3. The case of variable wind conditions on 14 September reveals the largest error (0.67) probably related to the ML erosion and the lack of accuracy in the optimal EVP retrieval on that day. Figure 6e also indicates a significant difference between the EVP retrieved by the variational method and KPP parameterization. This can be partly explained by the presence of inertial motions captured fairly well by ADCP measurements (not shown). The velocity shear, observed between the surface layer (10 m deep) and the subsurface layer dominated by the westward background current (NMC), creates the turbulence production, which maintains the viscosity at nearly constant level, compared to the KPP shape function which rapidly decays on the approach to the bottom of the mixed layer.

To further validate the obtained EVP estimates, the Ekman depth was assessed for two transects characterized by different wind forcing. Since the Ekman depth is proportional to $\nu^{1/2}$, and the estimated MLD-averaged viscosity values for the 11 and 13 September are 24 and 12 cm^2 s^{-1}, respectively (Table 1), we may expect a decrease of the Ekman depth value by a factor of $\sqrt{2}$ = 1.4 in 2 days, in response to the drop of the mean wind speed. Mixing relaxation should necessarily result in the MLD decrease, which was observed in the CTD data on 11 and 13 September. As it is seen from Fig. 3, the MLD decreased from 17 to 13 m (Table 1, column 6) thus providing an approximate ratio of 1.3, which is in a reasonably good agreement with the evolution of the Ekman layer depth predicted by the theory.

b. *Wind stress and Ekman currents*

The optimal EVPs and wind stress values for different transects have been used to compute individual (i.e., 5-min-averaged) Ekman current velocity profiles $\mathbf{u}_e(z)$ [Eq. (A2) of the appendix]. These velocity profiles and wind stress vectors (available at ~500-m resolution along the transects) were then averaged to yield the transect-mean values reported in Table 2 and shown in Fig. 7. In addition, we validated the optimal wind stress τ^{opt} against the value τ^* obtained from a bulk formulation and C_d parameterization (1) that depends on the wind speed at 10 m (U_{10}). The latter was deduced from meteorological observations at Porquerolles Island using a log-profile approximation with the roughness coefficient $z_0 = 2 \times 10^{-4}$ adopted from (Troen and Petersen 1989).

As it is seen from Table 2, the values of τ^{opt} appear to be low biased as compared to the values τ^* deduced from the bulk parameterization (1): The estimates of τ^* are close to the upper limits of the τ^{opt} standard deviations computed from their along-transect variability, whereas the time variation of both τ^{opt} and τ^* is reproduced fairly well (cf. Fig. 2). Similar estimates of the wind stress derived from the OCARINA platform (τ_O^*) demonstrate nearly identical time variation with larger mean values compared to τ^*. The difference between τ^{opt} (upper value) and τ^* did not exceed 10^{-2} N m^{-2} under moderate wind conditions, on 13 September. For milder winds, observed on 14 September, the agreement was

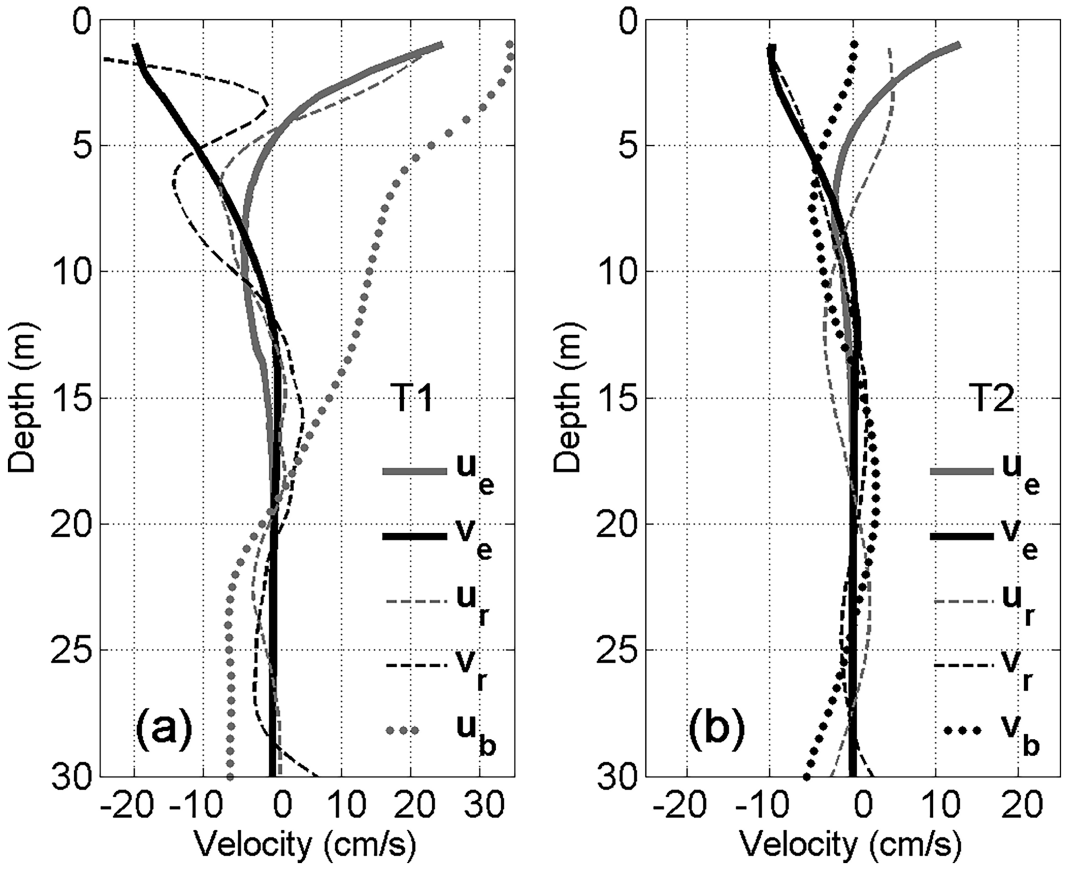

FIG. 7. Ekman velocity profiles ($\mathbf{u}_e$ and $\mathbf{v}_e$ components) on transects T1 and T2 (thick solid lines), errors of the background velocity approximation ($\mathbf{u}_r$ and $\mathbf{v}_r$; thin dashed lines), and the across-section background current velocities (dotted lines: $\mathbf{u}_b$ on T1 and $\mathbf{v}_b$ on T2), showing the two-layer circulation in the BoH. All profiles are transect averaged.

found even better. We attribute the low bias of the optimized wind stress to the relatively fast wind variations (Fig. 2) whose typical time scale was close to the adjustment time f^{-1} of the surface currents driven by Ekman dynamics. As a consequence, the turbulent mixing parameterized by the EVPs in Fig. 6 could not fully develop to correspond to the "nearly instant" winds directly observed at the meteorological station and by the OCARINA platform.

Wind-induced Ekman current velocities $|\mathbf{u}_e|^{\text{opt}}$ also show significant time variability in response to the wind. Close to the sea surface ($z = 1$ m), the velocity varies from 0.36 to 0.05 m s^{-1} demonstrating behavior similar to the wind stress (Table 2, columns 4 and 5). However, Ekman velocities on transects T2 and T3 appear to be low biased with respect to the values in column 5 derived from the empirical relationship of Weber (1983) between U_{10} and surface currents. Moreover, $|\mathbf{u}_e|^{\text{opt}}$ on T3 is smaller than that on T2, despite the wind speed being larger. The origin of this difference could be attributed to the lower optimized viscosity values in the eastern narrow. Indeed, in this part of the bay, the inflow background current in the surface mixed layer was opposing the eastward wind, thus making the EVP optimization less reliable. The angle between the optimal Ekman currents at the surface and the wind direction is found to be equal to 47°, 48°, and 65° for transects T1, T2, and T3, respectively. The first two values agree well with the value 45° for the direction difference between the surface current and the wind in the case of constant viscosity. Regarding parameterization of the surface current velocity, the estimation of $|\mathbf{u}_e|$ as a function of U_{10} [Eq. (2)] provided the values 39, 26, and 33 cm s^{-1} for transects T1–T3, respectively (Table 2, column 5). Only the surface velocity $|\mathbf{u}_e|$ obtained in the middle of the bay under the strongest wind (T1) satisfies the relationship of Weber (1983) established for steady wind conditions in the open ocean. The observations performed in the narrows (T2 and T3), where the wind and surface currents are constrained by orographic features, are less consistent with Weber's parameterization, indicating its limited applicability in the semienclosed basins like BoH under weak unsteady winds.

c. *Residual velocities*

After the Ekman profile reconstruction and subtraction, the background current velocities $\mathbf{u}_b$ were approximated by third-order polynomials and also subtracted from the

observed velocity profiles $\mathbf{u}_o(z)$. The resulting residual velocity $\mathbf{u}_r(z) = \mathbf{u}_o - \mathbf{u}_b$ is viewed as the background velocity error which contains contributions from unresolved processes (such as the Stokes drift) as well as the polynomial approximation error. The contribution of the Ekman current profiles $\mathbf{u}_e(z)$ (thick lines) to the residual currents (thin lines) is shown in Fig. 7. The overall relative error (err) of the optimization scheme is given in the last column of Table 2 and is defined by Eq. (5). For all transect-mean velocity data, the overall relative error of EVP retrieval (including the Ekman spiral reconstruction) is larger than 50%, with the maximum value (83%) corresponding to T4 on 14 September. The relatively large values of error are attributed to the fact that the proposed technique is aimed at retrieving the *mean* EVPs emerging in response to the vertical mixing induced by the variable winds. The resulting viscosity profiles, being fairly consistent with the existing parameterization schemes (Fig. 7), account only for a certain part of the turbulence-driven flow in the SBL, because the steady-state Ekman constraints are not entirely consistent with the highly variable wind conditions exposed in Fig. 2.

Inspection of the profiles in Fig. 7 also shows that larger residuals are observed in the surface layer, directly exposed to a combined forcing by wind and waves producing enhanced mixing. For the strong (Fig. 7a) and moderate (Fig. 7b) forcing (U_{10} = 12 and 8 m s^{-1}, respectively) the wind-induced currents constrained by the steady-state equations are qualitatively well approximated by the Ekman profiles emerging from the EVP retrieval algorithm in the upper 10 m of the water column. Residual velocity variations there could be attributed to the Stokes drift, Langmuir circulation, and the complex structure of the background current (Fig. 7, dotted line), not well reproduced by the polynomial approximation. A time lag between the wind-induced turbulent mixing and the current velocity adjustment can also contribute to the error.

Comparison of the background and Ekman current velocities is shown in Fig. 7. The two-layer background circulation pattern is clearly seen on T1 ($\mathbf{u}_b$ component), where the current velocity is fairly large (cf. right panel in Fig. 4), and less visible on T2 ($\mathbf{v}_b$ component), where the current was much weaker. The time evolution of the Ekman layer depth and MLD in response to changes in wind forcing is well reproduced. The depth of the background current reversal also changes between 11 and 13 September and appears to follow MLD evolution. These results provide an evidence of a complex circulation in the BoH, forced by large-scale upwelling motions and modulated by the wind and background currents.

5. Discussion and conclusions

Direct assessment of the vertical momentum transfer in the surface boundary layer requires finely tuned specialized equipment, such as microstructure profilers, and the use of sophisticated data processing techniques. As highlighted in the methodological study of Roget et al. (2006), getting accurate estimates of eddy diffusivity or dissipation rate of the turbulent kinetic energy in ocean environments remains a technically challenging task in observational oceanography. Moreover, microstructure profilers provide only snapshots of the turbulence field, which can vary significantly in space and time and, therefore, require extensive surveys to obtain robust estimates of the viscosity field at the horizontal scales of 0.1–1 km.

In this study, we demonstrate the feasibility of retrieving EVPs in the above spectral range from the velocity profiles observed by towed ADCP platforms. In comparison with microstructure profiling, velocity measurements by vessel-mounted or towed ADCPs are easy to perform and process. High-resolution and high-quality velocity profiles can be obtained for a wide variety of depth ranges, that cover both surface and bottom boundary layers, including the pycnocline [see Goddijn-Murphy et al. (2013) and Sentchev et al. (2020) for examples of towed ADCP surveying]. Towed platforms may also cover a wide range of wind and flow conditions. As a few examples, the vessel-towed ADCP measurements (Goddijn-Murphy et al. 2013) were used for monitoring tidal flow variations in the Pentland Firth (United Kingdom) where current velocities are among the highest (up to 5 m s^{-1}) on the globe; Li et al. (2004) employed towed ADCP observations to estimate bottom drag coefficient from space–time averaged velocity profiles in the Saint James tidal estuary, United States.

The data used in the present study were obtained under variable (4–12 m s^{-1}) winds which generated a complex circulation pattern partly driven by the Ekman transport in the semienclosed basin. The EV retrieval algorithm is based on the variational assimilation of the observed velocity profiles strongly constrained by the Ekman relationships. The vertically varying square root of the viscosity coefficient $\nu(z)$, and the wind stress were used as control/adjustable variables. The results demonstrate significant time variations of ν, whose magnitude and vertical structure are primarily driven by the wind. It is remarkable that this variability can be described by the parameterization of Pacanowski and Philander (1981) expressed in terms of the rational function of the Richardson number with coefficients dependent on the wind conditions: For winds exceeding 12 m s^{-1} the viscosity profile is well described by [Eq. (6)] with the conventional parameter set (ν_0 = 50 cm^2 s^{-1}, α = 5, and ν_b = 2 cm^2 s^{-1}) while for the winds in the range of 8–10 m s^{-1}, the optimal values of α and ν_b are, respectively, 3.5 and 4 cm^2 s^{-1}. For very low winds the proposed variational technique becomes inapplicable because the magnitude of Ekman currents falls below the level of observation errors due to the decay of the wind-driven turbulence in SBL.

Note that adjustable parameters may vary within a much larger range depending on the velocity shear and stratification conditions in the ambient flow. For instance, Forryan et al. (2013) found that ν_b = 10 cm^2 s^{-1} best fits the turbulent viscosity, estimated from microstructure profiles below the SBL in the equatorial undercurrent at high Richardson numbers. A significantly higher background viscosity is attributed to the contribution from unresolved processes occurring below the mixed layer, such as wave–wave interactions of the internal

wave field (Polzin et al. 1997), or wave–current interactions (Avicola et al. 2007).

Lozovatsky et al. (2006) analyzed microstructure profiles in the North Atlantic obtained under strong and more persistent wind conditions, resulting in a much deeper (50 m) mixed layer than observed in the present study. They proposed a EVP parameterization using certain combinations of the Richardson and Prandtl numbers for the background flows characterized by low ($\mathrm{Ri} < 0.1$) and intermediate ($\sim 0.25 < \mathrm{Ri} < \sim 2$) Richardson numbers.

An advantage of our approach to EVP retrieval from underway velocity measurements is a possibility to use continuous data acquisition and dense spatial coverage of the survey region by observations. Different sectors of the BoH (the bay interior, the narrows, and open sea) were sampled by the towed platform without any technical problems. This type of measurement technique is easy to implement and makes it possible to obtain velocity and EV profiles starting right underneath (1 m below) the sea surface. On the contrary, velocity and microstructure observations, targeted at EV estimations in the near-surface layer of the ocean from research vessels, demand special instrumentation (e.g., Soloviev et al. 1999) and techniques of data processing (Roget et al. 2006).

The dynamical constraints used for extracting the EVPs from observations are given by the basic steady-state Ekman balance, which fully develops at times larger than $f^{-1} \sim 3$ h for the depth-independent viscosity coefficient. However, our study indicates that the method does appear to be applicable for time intervals of a few hours. This feature can be partly attributed to the fact that the boundary layer adjustment/response to surface forcing tends to be shorter in the depth-dependent case (Madsen 1977). As mentioned above, the validity of the steady-state Ekman balance assumption is also supported by a reasonably good correspondence to empirical EVP parameterizations. In particular, the results were found to be fairly consistent with KPP parameterization: the maximum viscosity values were found at the depths of 5–6 m, corresponding to the maxima of the KPP shape function for the range of mixed layer thicknesses h of 13–17 m, independently diagnosed by the CTD casts on the days of the ADCP transects performed in stronger wind conditions.

It should also be noted that the proposed method is not designed for reconstructing the Ekman spiral per se: it is generally focused on extracting the mean EVPs in the SBL caused by variable winds. In these conditions, the Ekman spiral does not have enough time for the robust adjustment (e.g., Lewis and Belcher 2004; Wang and Kukulka 2021), whereas propagation and decay of the wind-driven turbulence respond to the changing wind much faster, providing realistic estimates of the transect-averaged EV profiles. The latter could be useful for improving the accuracy of diagnostic modeling in nearshore environments characterized by a complex bathymetry and variable wind forcing. In that respect, our results should be viewed as a method of obtaining an observational guidance to coastal modeling community for correctly parameterizing time variations of the mean eddy viscosities in SBL occurring under such complex environmental conditions at space and time scales of several kilometers and hours, respectively.

To further explore the effectiveness of the proposed method of EVP retrieval, it should be applied to a larger set of profiles, including profiles collected in deeper waters, not affected by coastal effects. Assessment of the eddy viscosity evolution in well stratified and deeper waters of the southern Bay of Biscay will be performed in our future study.

With a growing demand for development of the tidal-stream energy resource, monitoring of currents is routinely performed in the regions where the tidal flow is amplified by bathymetry providing large energy potential (e.g., Sentchev et al. 2018, 2020). As it was shown by Thiébaut et al. (2019), towed observation platforms provide an efficient tool for accurate assessment of the flow in these regions, contributing to and substantially improving the accuracy of modeling the extremely strong tidal currents, whose dynamics is balanced by dissipation. In this study, we demonstrate that underway velocity measurements by towed platforms can also provide valuable information for improvement of the turbulent momentum fluxes that will be particularly useful for modeling kinetic energy dissipation in tidally driven environments.

Acknowledgments. The data acquisition was performed during the UPCAST sea survey (https://doi.org/10.17600/17009500), funded by contracts with Ifremer Seyne-sur-mer, via the CNRS-INSU LEFE research program (TURBORADAR project) and the ANR program (TURBIDENT project). M. Y. was supported by the Office Naval Research (PARSEC project) and by the visiting scientist program of the University of Littoral (ULCO). We acknowledge the anonymous reviewers for the constructive comments which helped to improve the scientific quality of the paper.

Data availability statement. The ADCP, CTD, and wind data used during this study are openly available from the National Oceanographic Archive Data Center "ODATIS" at https://www.seanoe.org/data/00486/59768/.

APPENDIX

Variational Algorithm

To estimate the vertical variation of the vertical momentum diffusion coefficient $\nu(z)$, we minimized the following cost function:

$$J(\nu, \boldsymbol{\tau}) = \frac{1}{2}\left\{\int_d^0 \left[W_u(\mathbf{u} - \mathbf{u}_o)^2 + W_\nu(\nu - \nu^*)^2\right]dz + W_\tau(\boldsymbol{\tau} - \boldsymbol{\tau}_o)^2\right\} + \int_d^0 [\hat{\mathbf{E}}\mathbf{u}(z) - \boldsymbol{\tau}]\lambda(z)dz \tag{A1}$$

for each observed velocity profile $\mathbf{u}_o(z)$, and corresponding wind stress $\boldsymbol{\tau}_o$. The minimization was performed with respect to both $\nu(z)$ and the two components, τ_x and τ_y, of the wind stress vector $\boldsymbol{\tau}$. The weights W_u, W_ν, and W_τ in Eq. (A1) have the meaning of the inverse error variances in the observations of velocity, wind stress, and the respective

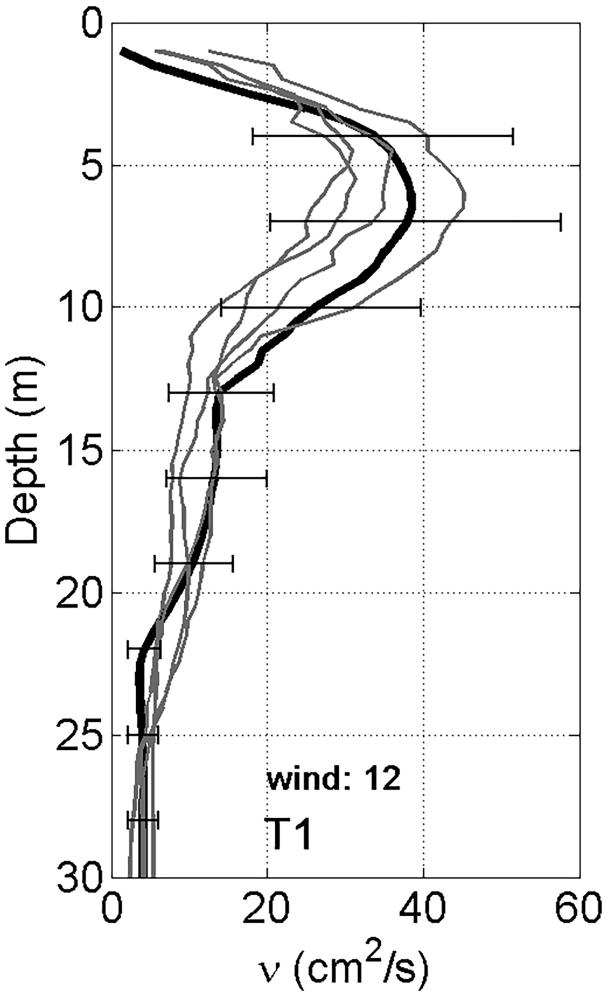

FIG. A1. Samples (gray lines) of the transect-averaged optimal EVP profiles obtained by simultaneously perturbing the observed velocity profiles along the transect T1, the wind stress on that date, and the first-guess value of the viscosity ν^*. The reference profile obtained without imposing the perturbations (Fig. 6a) is shown by the thick solid line.

first-guess value of the diffusion coefficient ν^*, which was assumed constant in the vertical. The integration is performed until the depth d is covered by the measurements. The last term in Eq. (A1) contains Lagrangian multipliers $\lambda(z)$ and constrains $\mathbf{u}(z)$ to be a solution of the Ekman problem:

$$[\partial_z \nu(z)\partial_z - f\mathbf{k}\times]\mathbf{u} = 0;\ \nu\partial_z\mathbf{u}|_0 = \boldsymbol{\tau};\ \partial_z\mathbf{u}|_d = 0, \tag{A2}$$

where f is the Coriolis parameter and $\mathbf{k}$ is the vertical unit vector. As a consequence, the discretized cost function (A1) implicitly depends only on $\nu(z)$ and $\boldsymbol{\tau}$ with $\hat{\mathbf{E}}\mathbf{u}(z) - \boldsymbol{\tau}$ symbolically representing the finite-difference form of the Ekman equations, Eqs. (A2).

To minimize (A1) with respect to $\nu(z)$ and $\boldsymbol{\tau}$, we first set to zero the gradients of J with respect to λ and $\mathbf{u}$:

$$\frac{\delta J}{\delta \lambda} = 0 : u = \hat{\mathbf{E}}^{-1}\boldsymbol{\tau}, \tag{A3}$$

$$\frac{\delta J}{\delta \mathbf{u}} = 0 : \lambda = W_u \hat{\mathbf{E}}^{-\mathrm{T}}(\mathbf{u} - \mathbf{u}_o), \tag{A4}$$

and then compute the gradients with respect to the control variables $\boldsymbol{\tau}$ and $\mu = \nu^{1/2}$ (used to maintain nonnegative property of ν during the descent):

$$\frac{\delta J}{\delta \boldsymbol{\tau}} = W_\tau(\boldsymbol{\tau} - \boldsymbol{\tau}_o) - \lambda(0), \tag{A5}$$

$$\frac{\delta J}{\delta \mu} = 2\mu[(\partial_z\lambda)(\partial_z\mathbf{u}) + W_\nu(\nu - \nu^*)]. \tag{A6}$$

Numerically, the optimization was performed with the double precision version of the quasi-Newtonian algorithm of Gilbert and Lemaréchal (1989). Due to moderate dimension of the problem, the Ekman matrix $\hat{\mathbf{E}}$ [representing finite-difference discretization of the left-hand sides in Eq. (A2)] was directly inverted at each iteration during the descent process.

To assess the method's sensitivity to variations of the observations and the first-guess values of the control variables, we conducted a series of numerical experiments by perturbing $\boldsymbol{\tau}_o$, $\mathbf{u}_o$, and ν^* while assuming that the results of optimization described in section 4 represent the reference (true) solution. The observed velocity profiles were perturbed by the white noise with standard deviations of 8 cm s^{-1} for each component of the observed velocity, 0.05 N m^{-2} for both components of $\boldsymbol{\tau}_o$, and 1 cm^2 s^{-1} for the first-guess value ν^* of the eddy viscosity coefficient. The results of these validation experiments (Fig. A1) demonstrated a reasonable agreement with the optimized EVPs variations, shown by the error bars in Fig. 6a and derived under the assumption of χ^2 statistics.

REFERENCES

Avicola, G. S., J. N. Moum, A. Perlin, and M. D. Levine, 2007: Enhanced turbulence due to the superposition of internal gravity waves and a coastal upwelling jet. *J. Geophys. Res.*, **112**, C06024, https://doi.org/10.1029/2006JC003831.

Belcher, S. E., and Coauthors, 2012: A global perspective on Langmuir turbulence in the ocean surface boundary layer. *Geophys. Res. Lett.*, **39**, L18605, https://doi.org/10.1029/2012GL052932.

Bourras, D., and Coauthors, 2019: Air-sea turbulent fluxes from a wave-following platform during six experiments at sea. *J. Geophys. Res. Oceans*, **124**, 4290–4321, https://doi.org/10.1029/2018JC014803.

Cao, A.-Z., H. Chen, W. Fan, H.-L. He, J.-B. Song, and J.-C. Zhang, 2017: Estimation of the eddy viscosity profile in the bottom Ekman boundary layer. *J. Atmos. Oceanic Technol.*, **34**, 2163–2175, https://doi.org/10.1175/JTECH-D-17-0064.1.

Chereskin, T. K., 1995: Direct evidence for an Ekman balance in the California Current. *J. Geophys. Res.*, **100**, 18 261–18 269, https://doi.org/10.1029/95JC02182.

Cushman-Roisin, B., L. Asplin, and H. Svendsen, 1994: Upwelling in broad fjords. *Cont. Shelf Res.*, **14**, 1701–1721, https://doi.org/10.1016/0278-4343(94)90044-2.

Flamant, C., 2003: Alpine lee cyclogenesis influence on air-sea heat exchanges and marine atmospheric boundary layer thermodynamics over the western Mediterranean during a tramontane/mistral event. *J. Geophys. Res.*, **108**, 8057, https://doi.org/10.1029/2001JC001040.

Forryan, A., A. P. Martin, M. A. Srokosz, E. E. Popova, S. C. Painter, and A. H. H. Renner, 2013: A new observationally motivated Richardson number based mixing parametrization for oceanic mesoscale flow. *J. Geophys. Res. Oceans*, **118**, 1405–1419, https://doi.org/10.1002/jgrc.20108.

Gilbert, J. C., and C. Lemaréchal, 1989: Some numerical experiments with variable-storage quasi-Newton algorithms. *Math. Program.*, **45**, 407–435, https://doi.org/10.1007/BF01589113.

Givon, Y., D. Keller Jr., V. Silverman, R. Pennel, P. Drobinski, and S. Raveh-Rubin, 2021: Large-scale drivers of the mistral wind: Link to Rossby wave life cycles and seasonal variability. *Wea. Climate Dyn.*, **2**, 609–630, https://doi.org/10.5194/wcd-2-609-2021.

Goddijn-Murphy, L., D. K. Woolf, and M. Easton, 2013: Current patterns in the Inner Sound (Pentland Firth) from underway ADCP data. *J. Atmos. Oceanic Technol.*, **30**, 96–111, https://doi.org/10.1175/JTECH-D-11-00223.1.

Guihou, K., J. Marmain, Y. Ourmieres, A. Molcard, B. Zakardjian, and P. Forget, 2013: A case study of the mesoscale dynamics in the north-western Mediterranean Sea: A combined data–model approach. *Ocean Dyn.*, **63**, 793–808, https://doi.org/10.1007/s10236-013-0619-z.

Jansá, A., 1987: Distribution of the mistral: A satellite observation. *Meteor. Atmos. Phys.*, **36**, 201–214, https://doi.org/10.1007/BF01045149.

Jones, J. H., 1973: Vertical mixing in the equatorial undercurrent. *J. Phys. Oceanogr.*, **3**, 286–296, https://doi.org/10.1175/1520-0485(1973)003<0286:VMITEU>2.0.CO;2.

Large, W. G., J. C. McWilliams, and S. C. Doney, 1994: Oceanic vertical mixing: A review and a model with a nonlocal boundary layer parameterization. *Rev. Geophys.*, **32**, 363–403, https://doi.org/10.1029/94RG01872.

Lewis, D. M., and S. E. Belcher, 2004: Time-dependent, coupled, Ekman boundary layer solutions incorporating Stokes drift. *Dyn. Atmos. Oceans*, **37**, 313–351, https://doi.org/10.1016/j.dynatmoce.2003.11.001.

Li, C., A. Valle-Levinson, L. P. Atkinson, K. C. Wong, and K. M. Lwiza, 2004: Estimation of drag coefficient in James River estuary using tidal velocity data from a vessel-towed ADCP. *J. Geophys. Res.*, **109**, C03034, https://doi.org/10.1029/2003JC001991.

Lozovatsky, I. D., E. Roget, H. J. S. Fernando, M. Figueroa, and S. Shapovalov, 2006: Sheared turbulence in a weakly stratified upper ocean. *Deep-Sea Res. I*, **53**, 387–407, https://doi.org/10.1016/j.dsr.2005.10.002.

Madsen, O. S., 1977: A realistic model of the wind-induced Ekman boundary layer. *J. Phys. Oceanogr.*, **7**, 248–255, https://doi.org/10.1175/1520-0485(1977)007<0248:ARMOTW>2.0.CO;2.

Marmain, J., A. Molcard, P. Forget, A. Barth, and Y. Ourmieres, 2014: Assimilation of HF radar surface currents to optimize forcing in the northwestern Mediterranean Sea. *Nonlinear Processes Geophys.*, **21**, 659–675, https://doi.org/10.5194/npg-21-659-2014.

Mellor, G. L., and T. Yamada, 1982: Development of a turbulence closure model for geophysical fluid problems. *Rev. Geophys.*, **20**, 851–875, https://doi.org/10.1029/RG020i004p00851.

Millot, C., 1999: Circulation in the western Mediterranean Sea. *J. Mar. Syst.*, **20**, 423–442, https://doi.org/10.1016/S0924-7963(98)00078-5.

Pacanowski, R. C., and S. G. H. Philander, 1981: Parameterization of vertical mixing in numerical models of tropical oceans. *J. Phys. Oceanogr.*, **11**, 1443–1451, https://doi.org/10.1175/1520-0485(1981)011<1443:POVMIN>2.0.CO;2.

Peters, H., M. C. Gregg, and J. M. Toole, 1988: On the parameterization of equatorial turbulence. *J. Geophys. Res.*, **93**, 1199–1218, https://doi.org/10.1029/JC093iC02p01199.

Polzin, K. L., J. M. Toole, J. R. Ledwell, and R. W. Schmitt, 1997: Spatial variability of turbulent mixing in the abyssal ocean. *Science*, **276**, 93–96, https://doi.org/10.1126/science.276.5309.93.

Roget, E., I. Lozovatsky, X. Sanchez, and M. Figueroa, 2006: Microstructure measurements in natural waters: Methodology and applications. *Prog. Oceanogr.*, **70**, 126–148, https://doi.org/10.1016/j.pocean.2006.07.003.

Sentchev, A., and M. Yaremchuk, 2016: Monitoring tidal currents with a towed ADCP system. *Ocean Dyn.*, **66**, 119–132, https://doi.org/10.1007/s10236-015-0913-z.

——, P. Forget, and P. Fraunié, 2017: Surface current dynamics under sea breeze conditions observed by simultaneous HF radar, ADCP and drifter measurements. *Ocean Dyn.*, **67**, 499–512, https://doi.org/10.1007/s10236-017-1035-6.

——, M. Yaremchuk, and M. Thiebaut, 2018: Monitoring strong tidal currents in straits and nearshore regions. *Ocean in Motion*, M. Velarde, R. Tarakanov, and A. Marchenko, Eds., Springer, 205–222.

——, T. D. Nguyen, L. Furgerot, and P. Bailly du Bois, 2020: Underway velocity measurements in the Alderney Race: Towards a three-dimensional representation of tidal motions. *Philos. Trans. Roy. Soc.*, **A378**, 20190491, https://doi.org/10.1098/rsta.2019.0491.

Smith, S. D., 1988: Coefficients for sea surface wind stress, heat flux, and wind profiles as a function of wind speed and temperature. *J. Geophys. Res.*, **93**, 15 467–15 472, https://doi.org/10.1029/JC093iC12p15467.

Soloviev, A., R. Lukas, P. Hacker, H. Schoeberlein, M. Baker, and A. Arjannikov, 1999: A near-surface microstructure sensor system used during TOGA COARE. Part II: Turbulence measurements. *J. Atmos. Oceanic Technol.*, **16**, 1598–1618, https://doi.org/10.1175/1520-0426(1999)016<1598:ANSMSS>2.0.CO;2.

Thiébaut, M., A. Sentchev, and P. Bailly du Bois, 2019: Merging velocity measurements and modeling to improve understanding of tidal stream resource in Alderney Race. *Energy*, **178**, 460–470, https://doi.org/10.1016/j.energy.2019.04.171.

Troen, I., and E. L. Petersen, 1989: *European Wind Atlas*. Risø National Laboratory, 656 pp.

Wang, X., and T. Kukulka, 2021: Ocean surface boundary layer response to abruptly turning winds. *J. Phys. Oceanogr.*, **51**, 1779–1794, https://doi.org/10.1175/JPO-D-20-0198.1.

Weber, J. E., 1983: Steady wind- and wave-induced currents in the open ocean. *J. Phys. Oceanogr.*, **13**, 524–530, https://doi.org/10.1175/1520-0485(1983)013<0524:SWAWIC>2.0.CO;2.

Yoshikawa, Y., and T. Endoh, 2015: Estimating the eddy viscosity profile from velocity spirals in the Ekman boundary layer. *J. Atmos. Oceanic Technol.*, **32**, 793–804, https://doi.org/10.1175/JTECH-D-14-00090.1.

Yu, L., and J. J. O'Brien, 1991: Variational estimation of the wind stress drag coefficient and the oceanic eddy viscosity profile. *J. Phys. Oceanogr.*, **21**, 709–719, https://doi.org/10.1175/1520-0485(1991)021<0709:VEOTWS>2.0.CO;2.

Yu, Z., and P. S. Schopf, 1997: Vertical eddy mixing in the tropical upper ocean: Its influence on zonal currents. *J. Phys. Oceanogr.*, **27**, 1447–1458, https://doi.org/10.1175/1520-0485(1997)027<1447:VEMITT>2.0.CO;2.

Zhang, Q., Y. Gao, and X. Lv, 2015: Estimation of oceanic eddy viscosity profile and wind stress drag coefficient using adjoint method. *Math. Probl. Eng.*, **2015**, 309525, https://doi.org/10.1155/2015/309525.

Zhang, Y., J. Tian, and L. Xie, 2009: Estimation of eddy viscosity on the South China Sea shelf with adjoint assimilation method. *Acta Oceanol. Sin.*, **28**, 9–16.